Mechanical Systems and Signal Processing 163 (2022) 108174

Contents lists available at ScienceDirect

Mechanical Systems and Signal Processing

journal homepage: www.elsevier.com/locate/ymssp

Shock-induced persistent contact and synchronous re-levitation control in an AMB-rotor system

Yixin Su [a,c], Yongpeng Gu [b,*], Patrick S. Keogh [c], Suyuan Yu [a], Gexue Ren [b]

[a] Department of Energy and Power Engineering, Tsinghua University, Beijing 100084, China
[b] School of Aerospace Engineering, Tsinghua University, Beijing 100084, China
[c] Department of Mechanical Engineering, University of Bath, Bath BA2 7AY, UK

ARTICLE INFO

Communicated by Paolo Pennacchi

Keywords:
Active magnetic bearing
Bi-stable phenomenon
Shock response
Re-levitation control
Phase search

ABSTRACT

Active magnetic bearings (AMBs) have limited dynamic load capacity due to magnetic saturation. Hence, large external disturbances (such as shock loads) may cause contact between the rotor and touchdown bearings (TDBs), which may evolve into complex dynamic behaviour and damage the machine. This paper considers the shock responses of a rotor and viable re-levitation control options when the AMB is still functional. Bi-stable responses and shock-induced persistent forward rubbing were observed in an experimental AMB-flexible rotor facility and its numerical model. The analytical solution for steady synchronous motions with rubbing of a general AMB-flexible rotor system was proposed. The standard control action for a contact-free rotor state would not be appropriate due to phase changes and the displacement amplitude differences in the frequency responses. To destabilise the persistent contact responses and restore contact-free levitation, open-loop phase search based synchronous compensation (PSSC) control and synchronous motion compensation (SMC) control are designed, which are activated when a persistent contact is detected. Stability of the control system and the effectiveness of these two re-levitation control methods are verified by simulation and experimental results. It is also found by comparison that the efficiency of PSSC depends on the phase difference (incorrect phases may degrade rotor response), while the SMC consumes more computing effort.

1. Introduction

Interactions between a rotor and touchdown bearing (TDB), caused by large external disturbances or overloads, can result in problematic dynamic behaviours of the rotor in active magnetic bearings (AMBs) system [1]. The control structure is expected to work predictively in order to prevent the rotor contacts. However, due to the limited AMB forces and high-g shock loads in special application fields [2], the contact between the rotor and TDBs is inevitable and persistent contact may be induced under certain dynamic conditions. Prolonged exposure to these severe dynamic conditions will cause the degradation of TDBs, requiring regular replacements. This leads to outage periods that are costly in terms of missed productivity [3]. Therefore, a clear aim is to restore contact-free levitation through available control capability in an efficient manner. This would be beneficial for maintaining the normal operation of the maglev rotor under shock loads and for extending the life of the TDB [4].

* Corresponding author.
E-mail addresses: syx16@tsinghua.org.cn (Y. Su), guyp@tsinghua.edu.cn (Y. Gu), enspsk@bath.ac.uk (P.S. Keogh), suyuan@tsinghua.edu.cn (S. Yu), rengx@tsinghua.edu.cn (G. Ren).

https://doi.org/10.1016/j.ymssp.2021.108174
Received 28 November 2020; Received in revised form 24 May 2021; Accepted 18 June 2021
Available online 7 July 2021
0888-3270/© 2021 Elsevier Ltd. All rights reserved.

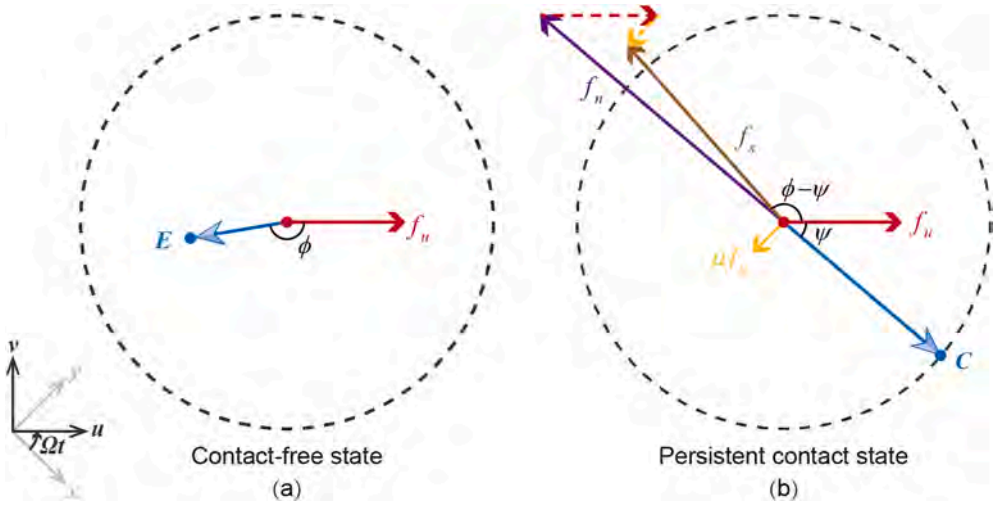

Fig. 1. Synchronous orbits viewed in a synchronously rotating reference frame: (a) contact-free orbit E induced by the unbalance force f_u; (b) persistent contact orbit C induced by unbalance force f_u, normal contact force f_n, tangential friction force μf_n, and resultant AMB force f_s.

Accordingly, a fuller understanding of rotor dynamic behaviours in rotor/TDB contact conditions is necessary. Most related studies have dealt with the rotor dynamics during the drop event. This is essentially a purely passive dynamic process, as it is considered that all control capability associated with an AMB no longer exists. Modelling, simulations, and tests on an industrial scale have been undertaken [5–8], and detailed predictions have become possible.

However, the coupling of functional AMBs makes the dynamic behaviour of a rotor more complex. Keogh and Cole [4] analysed the variable contact mode and stability of AMB-rotor systems. Simulation and experiment results indicated that changes in synchronous vibration amplitude and phase induced by contact events cause existing controllers to be ineffective in attenuating rotor displacements [9]. Some of the issues that should be considered when assessing rotor dynamic coupling with contact events [10]. For some special operating conditions, an AMB-rotor system has two stable periodic solutions: one without contact and the other involving persistent contact. This is called bi-stable phenomenon, which is a theoretical definition and is different from a stable operation in the usual industrial specification. With external disturbances, the rotor motion may develop to the point where initial rotor bouncing continues and transgresses into persistent rubbing (or combined bounce and rub), or even to the point of becoming chaotic unless further control action is taken or other inputs are applied [3]. Keogh and Cole [11] presented the analytical solution of synchronously persistent contact motions for a simple symmetric AMB-rigid rotor system. The solution for a general AMB-flexible rotor system has not been given in the literature.

It is desirable to destabilise such persistent contact because it will cause an accumulation of damage and limit TDB life. Further, as inherent unbalance may be the main factor for persistent contact, some synchronous unbalance force compensation-based controllers have been studied [12]. Phase changes caused by contact also need to be considered, and some robust control related algorithms have been proposed [13,14]. Ulbrich et al. [15] considered electromechanical actuation of a TDB, while Cade et al. [16] and Li et al. [17] implemented piezoelectric actuation for a TDB. The option of an active TDB offers additional control capabilities with the potential of restoring contact-free rotor levitation. However, an active TDB involves a more complex structure and would incur higher costs.

To date, there is a lack of published work relating to shock response and its corresponding automatic re-levitation control of AMB-rotor systems. Jarroux et al. [18–20] investigated the dynamic behaviour of an AMB-rotor system with strong base motions. The 6,000 rpm rotor, which was placed on a shock platform and experienced sinusoidal disturbance (0.1–1.1 G amplitude at 20 Hz), returned to a stable state after rubbing with the TDBs for a short time. Nonlinear dynamic behaviours and parameter analysis of an AMB-rotor system subjected to strong base shock excitation have been studied by numerical simulation [21]. No automatic re-levitation control has been designed and applied for shock contact in the above researches. Hawkins et al. [22] presented the floating shock platform test results for an AMB supported chiller compressor for MIL-S-901D shock certification. After experiencing limited contact time between the rotor and TDBs, the AMBs underwent a quick restart and the rotor returned to a stable operating state. However, considering large turbomachinery such as those in nuclear plants [23–25], the time to restart and recover nominal operating conditions can be very long. If some structural damages occurred, maintenance implies non negligible costs.

The aim of this paper is to provide an understanding of the bi-stable phenomenon and possible contact faults caused by shock loads in an AMB-rotor system. This is achieved through analytical expressions, nonlinear dynamic simulations, and experimental results from an AMB-flexible rotor facility. Then, an open-loop phase search based synchronous compensation (PSSC) control and a synchronous motion compensation (SMC) control methods are designed and applied, respectively, to destabilise the limit cycle responses. Comparisons between these two control actions are also discussed with relevance to implementation. The new aspect of this paper is that it provides insights into shock contact in the bi-stable zone and enables real-time detection and online control actions to stabilise contact-free operation of the rotor, even in the event of shock loads.

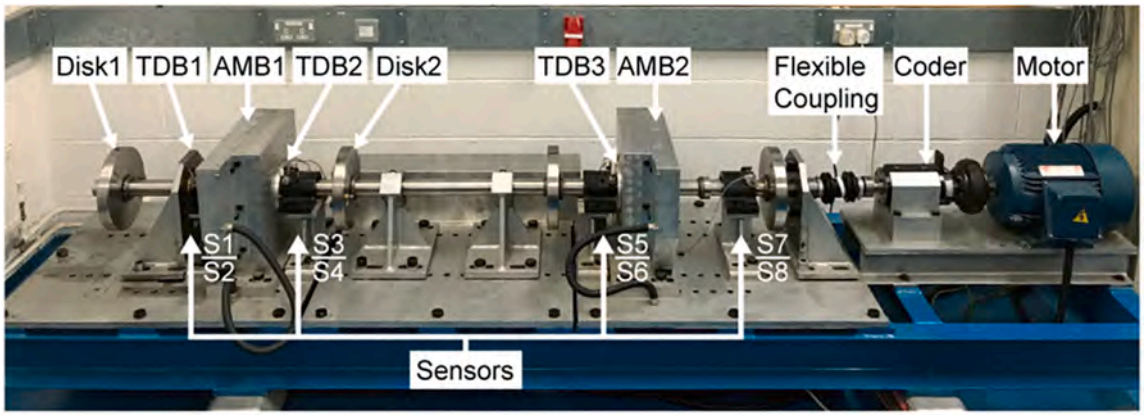

Fig. 2. AMB-flexible rotor facility.

2. Bi-stable phenomenon

2.1. Conditions for bi-stable phenomenon

First, a symmetric AMB-rigid rotor system is taken to illustrate the bi-stable phenomenon theoretically. The rotor is modelled as a point mass. The synchronously rotating reference frame (u,v) is used to analyse the existence of persistent contact clearly. In Fig. 1, the left view (a) is a contact-free case that the unbalance and synchronous AMB forces under a proportional-integral-derivative (PID) control drive the rotor to the point E with a phase angle ϕ. This point lies within the clearance circle. The phase angle between the force and response ϕ is determined by the AMB characteristics, the unbalance mass, and the rotational speed. The right view (b) shows a rotor in forward synchronous rubbing. The rotor is driven to the point C with a phase angle ψ on the clearance circle under the effect of the unbalance force f_u, the normal contact force f_n, the tangential friction force μf_n, and the resultant synchronous AMB force f_s. If these forces are balanced, a persistent contact may occur, which means that bi-stable responses exist.

For a symmetric AMB-rigid rotor system, previous studies have proved that the bi-stable responses may exist when the angle ψ satisfies Eq. (1) [11]:

$$\begin{cases} \dfrac{f_n}{f_u} = \dfrac{1}{(1+i\mu)}\left(e^{i\psi} - \dfrac{c}{r_E}e^{i\phi}\right) \\ \mathrm{Im}\left(\dfrac{f_n}{f_u}\right) = 0 \\ \mathrm{Re}\left(\dfrac{f_n}{f_u}\right) \rangle 0 \end{cases}, \tag{1}$$

where μ is the friction coefficient, c is the maximum gap between the rotor and the TDB, and r_E is the steady motion radius of the non-contacting orbit.

However, it is difficult to find the theoretical persistent contact solution for an AMB-flexible rotor system by the way of Keogh and Cole [11] due to the phase differences of motions at different axial positions of a flexible rotor. In this work, a new derivation of the theoretical persistent contact solution for a general AMB-flexible rotor system is given in the next section.

2.2. Experimental study

The experimental AMB-flexible rotor facility is shown in Fig. 2. The rotor is mounted horizontally on two radial AMBs. Eight current-controlled pulse width modulated amplifiers power the magnet coils with a bias current of 4.3 A, giving an open-loop bearing negative stiffness of 2×10^6 N/m, a current gain of 487 N/A, and a peak filter control force of approximately 1,500 N. Local PID displacement feedback control of the bearings provided stable rotor levitation and modal damping. The motor were controlled by a frequency converter.

The rotor shaft is 2 m long with four 10 kg disks of radii 10 cm mounted on it to provide added inertia, giving a total mass of 100 kg. The first forward and backward flexural mode critical speeds are 25.3 Hz and 26.5 Hz, respectively. The rotor is driven through a flexible coupling by a motor whose maximum rotational speed is 6,000 rpm. The residual unbalance of the rotor is approximately equivalent to 3,600 g·mm at Disk 2. In the experiments, a 64 g unbalance mass was added to Disk2, located at 100 mm from the centre of the disk in the same phase as the equivalent residual unbalance, giving a total of 10^4 g·mm.

Three TDBs are configured, as shown in Fig. 2. Rolling element bearings (TDB2 and TDB3) with a nominal radial clearance (0.7 mm) prevent contact between the AMB laminations and the rotor, which have a radial clearance of 1.2 mm. Additionally, a bronze

shiraz.barg@gmail.com

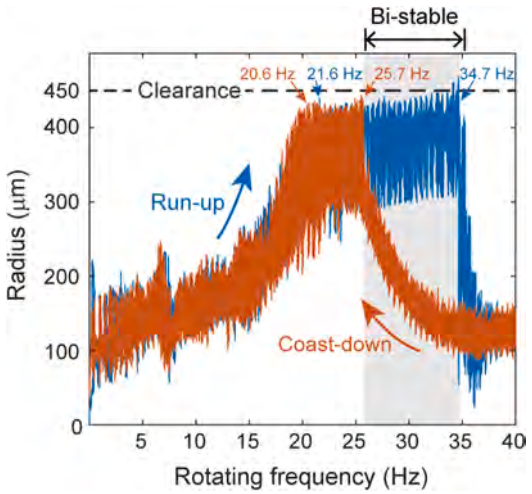

Fig. 3. Experimental radial displacements of rotor measured by S1 and S2 with gradual increase and decrease of the rotating frequency and 10^4 g·mm unbalance on Disk2.

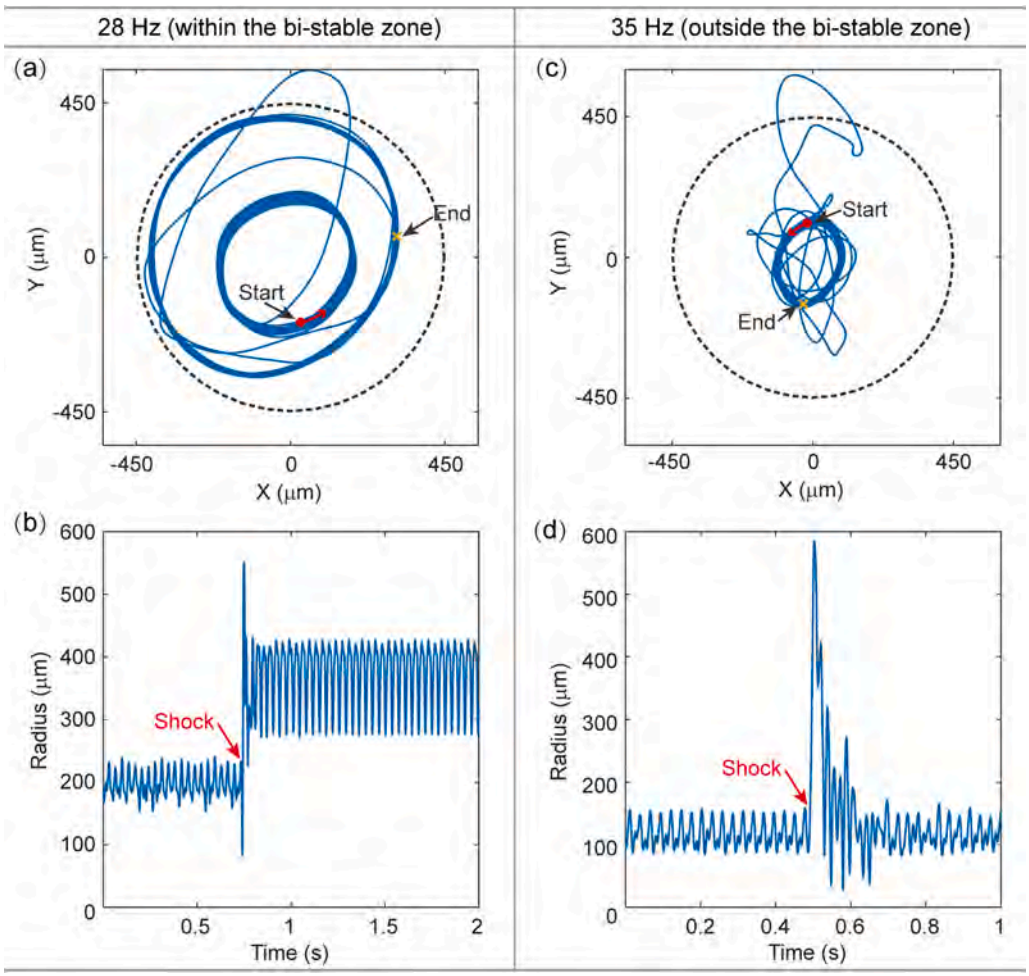

Fig. 4. Experimental results of shock responses measured by S1 and S2: (a) and (c) rotor trajectories for shock responses with initial running frequencies of 28 and 35 Hz, respectively; (b) and (d) the corresponding motion radii.

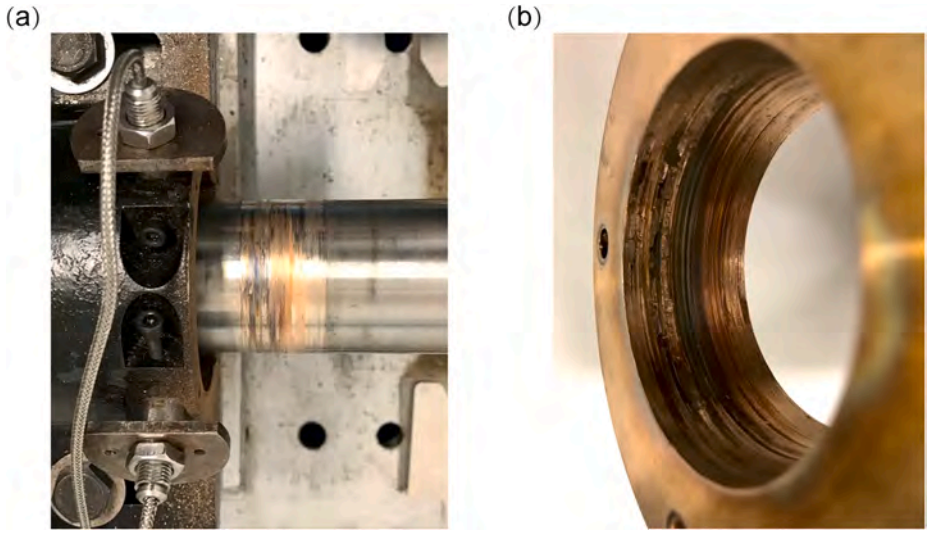

Fig. 5. Damage to the rotor (a) and the TDB (b) caused by persistent contacts at 30 Hz.

bushing (TDB1 with a nominal radial clearance of 0.45 mm) is located close to the rotor disks to further prevent rotor excursions.

Lateral displacements of the rotor are measured using eight eddy current displacement sensors in four axial planes, as shown in Fig. 2. Each sensor pair is arranged at $\pm 45^{\circ}$ either side of vertical. The Sensor pairs S3/S4 and S5/S6 are used for the controls of AMB1 and AMB2, respectively. Besides, the sensor pair S1/S2 is used to monitor the motions of rotor near TDB1. The distance between TDB1 and S1/S2 is 7 cm due to the restriction of mounting holes.

To obtain dynamic conditions of the bi-stable without/with contact phenomenon of the AMB-rotor facility by experiments, the rotating frequency was slowly increased from 0 to 40 Hz and then reduced at a similar rate. Fig. 3 shows the synchronous frequency response measurements undertaken in the plane of the sensor pair S1/S2 associated with TDB1. It can be seen that the rotor radial displacement measured by S1 and S2 increases with frequency up to 20.6 Hz (due to system resonance) until the rotor being in contact with TDB1. Below this rotational speed, the rotor was not in contact with TDB1. Increasing the rotating frequency above 20.6 Hz through to 34.7 Hz drives the rotor into contact with TDB1, with rotor radial displacements at the S1/S2 plane of approximately 0.4 mm. Beyond 34.7 Hz through to 40 Hz, the contact is lost and the rotor radial displacement drops to a post-resonance level. The forcing frequency was then decreased and contact was experienced only from 25.7 Hz to 20.6 Hz. This hysteresis effect in the system response arises from the nonlinear characteristics of the rotor/AMB/TDB system. This clearly shows evidence of bi-stable responses from 25.7 to 34.7 Hz, with and without rotor/TDB contact. When in persistent contacts, the non-collocation between S1/S2 and TDB1 results in a reduction of rotor motion radius at the S1/S2 position.

2.3. Potential trigger condition – shock loads

Although steady persistent contact may exist, the conditions of its occurrence (from point *E* to *C* in Fig. 1) remain unclear. The amplitude of the rotor's synchronous frequency response is generally designed to be within the gap between the rotor and TDB; hence, rotor-TDB contact conditions do not exist. However, shock loads that rotating machines (especially onboard machines) may encounter during normal operation can lead to contact between the rotor and the TDBs, resulting in complex nonlinear vibrations and machine damage [18,21,26]. Therefore, it is necessary to investigate shock-induced contact response.

For the AMB-flexible rotor bearing facility with the amplitude-frequency characteristics presented previously, an instantaneous shock force was applied to the rotor by applying current impulses to both AMBs. This was conducted when the rotor was running at different rotating speeds in contact-free conditions. The current impulse was in the form of a half-sine signal with an amplitude of 3 A and a period of 12 ms. Experimental results indicated that shock loads can cause persistent rotor contact in the bi-stable zone (from a red point to a blue point in the bi-stable zone in Fig. 3). Moreover, the larger the whirl radius before the shock, the easier it is to jump to a stable contact mode response.

Fig. 4(a) and (b), respectively, present the rotor trajectory and corresponding radius measured by S1 and S2 for shock responses with an initial rotating frequency of 28 Hz. Under the effect of inherent unbalance, the rotor whirled in the forward sense with a very small motion radius of 0.2 mm before the shock was applied. After the shock input, the rotor bounced sharply, which then evolved into a persistent contact (forward rubbing) under the combined action of the unbalanced force, nonlinear electromagnetic force, normal restoring force, and tangential dry friction. The motion radius fluctuated around the maximum gap value, and the frequency spectrum analysis indicated that the forward rubbing motion and rotational speed were at the same frequency.

Fig. 4(c) and (d), respectively, present the rotor trajectory and corresponding radius measured by S1 and S2 for shock responses with an initial rotating frequency of 35 Hz. Like the previous section, under the effect of inherent unbalance, the rotor whirled forward with a very small motion radius of motion of 0.1 mm before the shock, and the rotor vibrated sharply when the shock was applied.

shiraz.barg@gmail.com

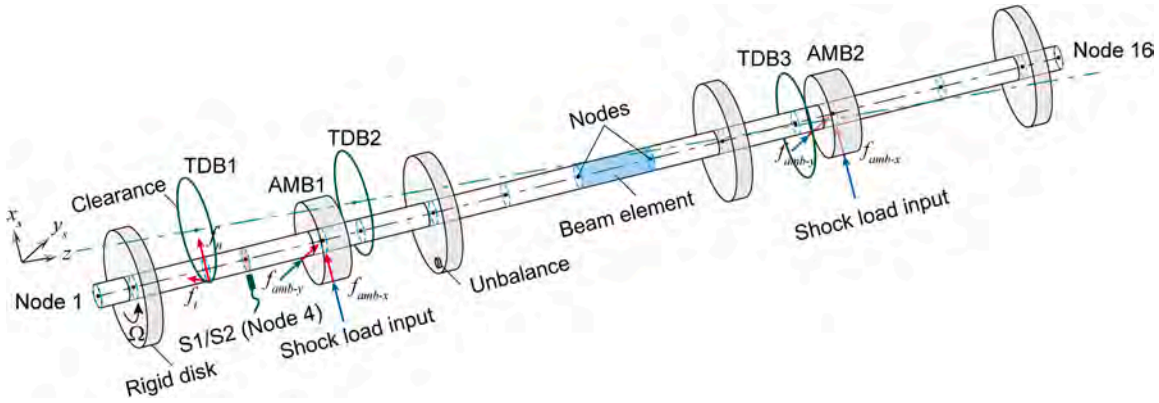

Fig. 6. Finite element model of the AMB-flexible rotor facility considering rotor/TDB contact.

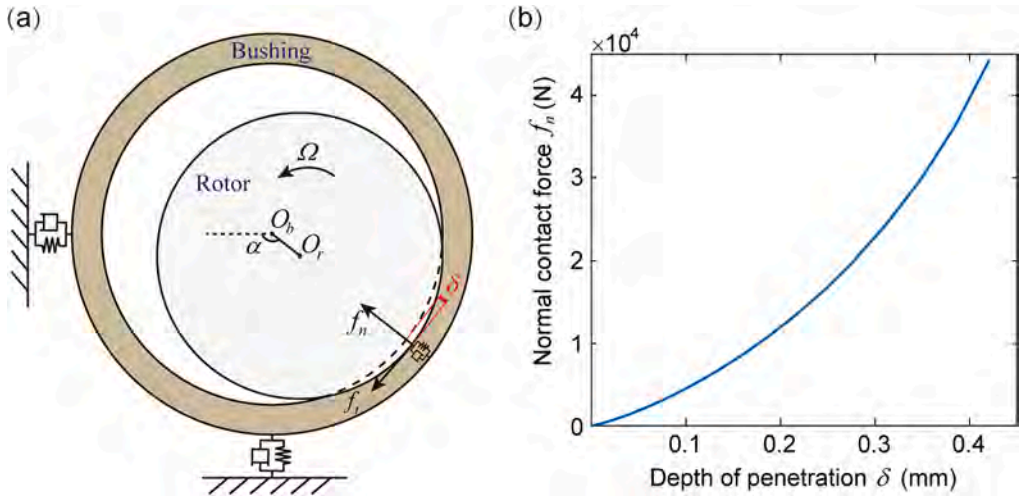

Fig. 7. (a) Rotor/TDB contact model; (b) Empirical model of the nonlinear contact force/deflection relation.

However, the shock contact time was short and the rotor then gradually recovered to become contact-free at the centre with the original whirl radius.

Therefore, a shock load is one of the potential trigger conditions that may cause persistent contact. As contact continues, the TDB and the rotor will be severely worn or even deformed due to persistent contact, dry friction, and thermal effects. Fig. 5 shows the damage to the rotor and TDB caused by contact experiments with a total contact time of no more than 1 min. The experimental results demonstrate the potential hazards caused by shock disturbances to the rotor under bi-stable operating conditions.

3. Dynamic modelling and simulation

3.1. Rotor/AMB/TDB system

As shock contact experiments are destructive, a nonlinear dynamic model was built to investigate the shock contact and re-levitation control problems. The shaft is divided into 15 beam elements using the finite element methodology of Nelson and McVaugh [27], as shown in Fig. 6. The unbalance forces, AMB forces, contact forces and shock loads were applied to the corresponding nodes. The measurement plane of the sensor pair S1/S2 associated with TDB1 is shown in Fig. 6.

The AMB force components in the x- and y-axes applied to the rotor at corresponding nodes are written as follows:

$$f_{amb-\gamma} = \frac{k_f}{k_s}\left(\frac{\tanh\left(k_s(I_0+I_c)^2\right)}{(c-\gamma)^2} - \frac{\tanh\left(k_s(I_0-I_c)^2\right)}{(c+\gamma)^2}\right), \tag{2}$$

where $\gamma = x_r$ or y_r denotes the rotor displacement from the AMB magnetic centre, and c is the effective magnetic gap. The bias and control currents (I_0 and I_c) are direction dependent. The AMB stator and rotor iron will have a magnetic flux saturation limit, which is

represented empirically by the *tanh* function, resulting in a maximum AMB radial force of k_f/k_s, where $k_f = \mu_0 N^2 A$ and k_s is a saturation constant.

Since the AMB system is inherently unstable, a PID controller is applied to realise stable rotor levitation by calculating the control current based on the error between the reference value and the signal from the displacement transducer.

The rotor/TDB contact model in the contact plane is drawn in Fig. 7(a). O_b and O_r are geometric centre of the TDB and the rotor, respectively. The TDB is of the bushing type and is supported by high stiffness springs and dampers. The contact state between the rotor and the TDB depends on the penetration δ. When $\delta > 0$, the rotor will be subjected to a normal restoring contact force f_n and tangential contact force f_t. The contact force vector containing the normal restoring force and tangential friction is given by

$$\begin{bmatrix} f_{c,x} \\ f_{c,y} \end{bmatrix} = \begin{bmatrix} -\cos\alpha & \sin\alpha \\ -\sin\alpha & -\cos\alpha \end{bmatrix} \begin{bmatrix} f_n \\ f_t \end{bmatrix}. \tag{3}$$

The nonlinear normal restoring contact force/deflection relation is contained by an empirical model, as shown in Fig. 7(b). A smooth Coulomb friction model, which is a variation of the classic Coulomb model, is adopted here to avoid any numerical difficulties. The friction force f_t is calculated by

$$f_t = -\tanh\left(\frac{v_r}{v_s}\right) \cdot \mu f_n, \tag{4}$$

where μ is the friction coefficient and set as 0.15 to represent the sliding conditions between the steel rotor and bronze bushing. The term v_s is the velocity tolerance and the term v_r is the relative speed at the contact point between the rotor and TDB, which can be calculated as

$$v_r = \Omega \cdot r + v_t, \tag{5}$$

where $v_t = (\dot{y}_r - \dot{y}_b)\cos\alpha - (\dot{x}_r - \dot{x}_b)\sin\alpha$, and $\alpha = \arctan\left(\frac{y_r - y_b}{x_r - x_b}\right)$.

The unbalanced force vector under varying speed conditions is given by

$$\begin{bmatrix} f_{u,x} \\ f_{u,y} \end{bmatrix} = me\dot{\varphi}^2 \begin{bmatrix} \cos\varphi \\ \sin\varphi \end{bmatrix} + me\ddot{\varphi} \begin{bmatrix} \sin\varphi \\ -\cos\varphi \end{bmatrix}, \tag{6}$$

where φ is the rotational angle of the rotor. The second term in Eq. (6) is in the tangential direction and refers to changes in the magnitude of velocity of the unbalance.

Finally, the governing equation of the system can be written in a matrix–vector form as follows [28]:

$$\mathbf{M}\ddot{\mathbf{q}} + (\mathbf{C}_f + \dot{\varphi}\mathbf{G})\dot{\mathbf{q}} + (\mathbf{K}_f + \ddot{\varphi}\mathbf{K}_{ST})\mathbf{q} = \mathbf{f}_u + \mathbf{f}_{amb} + \mathbf{f}_c, \tag{7}$$

where, $\mathbf{q}$ is the generalised coordinate vector of finite element nodes; $\mathbf{M}, \mathbf{K}_f, \mathbf{C}_f$ and $\mathbf{G}$ are the global mass, structural stiffness, damping and gyroscopic matrices; $\mathbf{K}_{ST}$ is the stiffness matrix for transient motions; $\mathbf{f}_u, \mathbf{f}_{amb}$ and $\mathbf{f}_c$ are the global unbalance force, AMB force, and contact force vectors, respectively.

3.2. Solution for steady synchronous motions with rubbing

In order to theoretically confirm the forward synchronous rubbing in an AMB-flexible rotor system with bushing type TDBs, the analytical solution for steady synchronous motions with rubbing is presented in this subsection.

Here the rotational speed of the rotor is constant and is designed as Ω. The movement of the TDB is ignored because of a very high support stiffness. The AMB forces are linearized and modelled by the stiffness and damping coefficient matrices. Then the equation of motion for the system can be written as:

$$\mathbf{M}\ddot{\mathbf{q}} + \mathbf{C}\dot{\mathbf{q}} + \mathbf{K}\mathbf{q} = \mathbf{f}_{\text{ext}}, \tag{8}$$

where the matrices $\mathbf{C}$ and $\mathbf{K}$ contain the contributions of both the rotor and the AMBs, and $\mathbf{f}_{\text{ext}}$ is the external force vector.

Assuming that the node with index k is in a steady forward rubbing orbit at the corresponding TDB, we have $x_k = c\cos(\Omega t + \phi)$ and $y_k = c\sin(\Omega t + \phi)$, where ϕ is the phase angle. Let $\mathbf{q}_1 = [x_k, y_k]^{\mathrm{T}}$ denote the translational degrees of freedom of node k, and $\mathbf{q}_2$ denote the generalised coordinate vector that consists of the rest degrees of freedom. Note that the node k only subject to the contact force, and the rest nodes only subject to unbalanced force. Hence, the governing equation of the system can be rewritten in the following partitioned form:

$$\begin{bmatrix} \mathbf{M}_{11} & \\ & \mathbf{M}_{22} \end{bmatrix} \begin{bmatrix} \ddot{\mathbf{q}}_1 \\ \ddot{\mathbf{q}}_2 \end{bmatrix} + \begin{bmatrix} \mathbf{C}_{11} & \mathbf{C}_{12} \\ \mathbf{C}_{21} & \mathbf{C}_{22} \end{bmatrix} \begin{bmatrix} \dot{\mathbf{q}}_1 \\ \dot{\mathbf{q}}_2 \end{bmatrix} + \begin{bmatrix} \mathbf{K}_{11} & \mathbf{K}_{12} \\ \mathbf{K}_{21} & \mathbf{K}_{22} \end{bmatrix} \begin{bmatrix} \mathbf{q}_1 \\ \mathbf{q}_2 \end{bmatrix} = \begin{bmatrix} \mathbf{f}_c \\ \mathbf{f}_u \end{bmatrix} \tag{9}$$

Using Euler's formula, sine and cosine can be expressed in terms of the exponential function to simplify the derivation, and we have

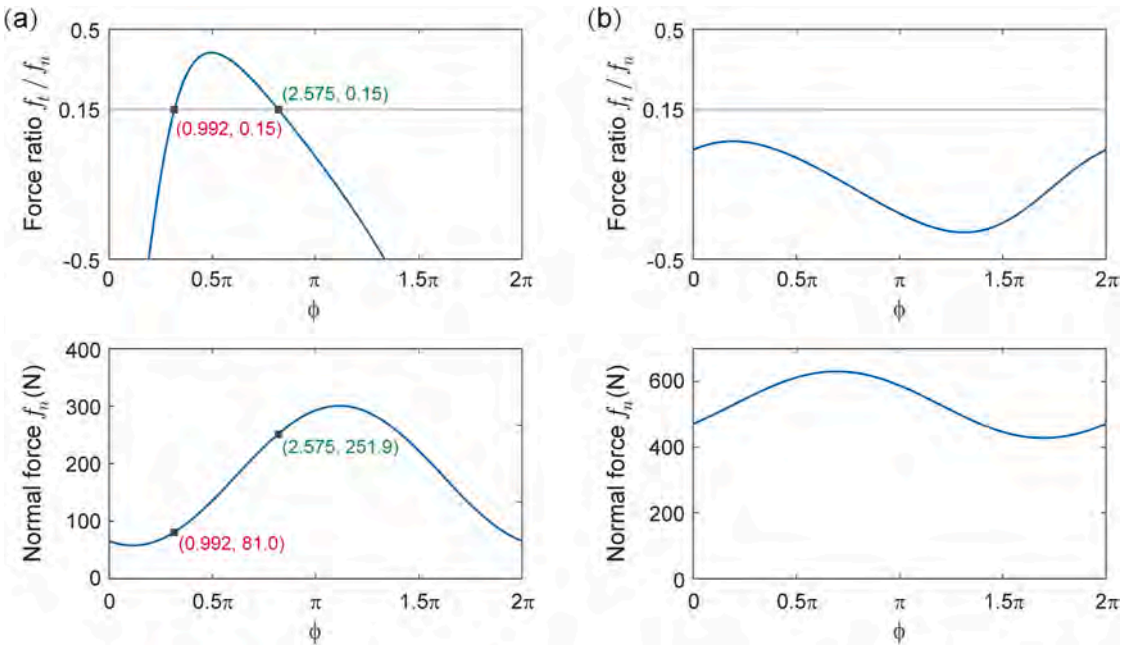

Fig. 8. Plots of the contact forces versus the phase angle: (a) the curves at 28 Hz; (b) the curves at 35 Hz.

$$\mathbf{q}_1 = c\begin{bmatrix}\cos(\Omega t+\phi)\\ \sin(\Omega t+\phi)\end{bmatrix} = \frac{c}{2}\begin{bmatrix}e^{i(\Omega t+\phi)}+e^{-i(\Omega t+\phi)}\\ -ie^{i(\Omega t+\phi)}+ie^{-i(\Omega t+\phi)}\end{bmatrix} = \frac{c}{2}e^{i\phi}\begin{bmatrix}1\\ -i\end{bmatrix}e^{i\Omega t}+\frac{c}{2}e^{-i\phi}\begin{bmatrix}1\\ i\end{bmatrix}e^{-i\Omega t}. \tag{10}$$

The equation above can be written in the form as $\mathbf{q}_1 = \mathbf{Q}_1 e^{i\Omega t} + \overline{\mathbf{Q}}_1 e^{-i\Omega t}$. Similarly, the unbalanced force at a constant speed can be written as

$$\begin{bmatrix}f_{u,x}\\ f_{u,y}\end{bmatrix} = me\Omega^2\begin{bmatrix}\cos\Omega t\\ \sin\Omega t\end{bmatrix} = \frac{me\Omega^2}{2}\begin{bmatrix}1\\ -i\end{bmatrix}e^{i\Omega t}+\frac{me\Omega^2}{2}\begin{bmatrix}1\\ i\end{bmatrix}e^{-i\Omega t}. \tag{11}$$

So that the global unbalanced force vector can be written as $\mathbf{f}_u = \mathbf{F}e^{i\Omega t} + \overline{\mathbf{F}}_2 e^{-i\Omega t}$.

It is simply assumed that the solution $\mathbf{q}_2$ also has the form of $\mathbf{Q}_2 e^{i\Omega t} + \overline{\mathbf{Q}}_2 e^{-i\Omega t}$. Substituting the exponential form representations for $\mathbf{q}_1, \mathbf{q}_2$ and $\mathbf{f}_u$ into the second row of Eq. (9) gives

$$\left[-\Omega^2\mathbf{M}_{22}+i\Omega\mathbf{C}_{22}+\mathbf{K}_{22}\right]\mathbf{Q}_2 = \mathbf{F}_u - \left(-\Omega^2\mathbf{M}_{21}+i\Omega\mathbf{C}_{21}+\mathbf{K}_{21}\right)\mathbf{Q}_1 \tag{12}$$

$$\left[-\Omega^2\mathbf{M}_{22}-i\Omega\mathbf{C}_{22}+\mathbf{K}_{22}\right]\overline{\mathbf{Q}}_2 = \overline{\mathbf{F}}_u - \left(-\Omega^2\mathbf{M}_{21}-i\Omega\mathbf{C}_{21}+\mathbf{K}_{21}\right)\overline{\mathbf{Q}}_1 \tag{13}$$

For a given value of the phase angle ϕ, Eqs. (12) and (13) are solved to determine $\mathbf{Q}_2$ and $\overline{\mathbf{Q}}_2$. Then the contact force can be calculated by the first row of Eq. (9) as $\mathbf{f}_c = \mathbf{F}_c e^{i\Omega t} + \overline{\mathbf{F}}_c e^{-i\Omega t}$, with:

$$\mathbf{F}_c = \left(-\Omega^2\mathbf{M}_{11}+i\Omega\mathbf{C}_{11}+\mathbf{K}_{11}\right)\mathbf{Q}_1 + \left(-\Omega^2\mathbf{M}_{12}+i\Omega\mathbf{C}_{12}+\mathbf{K}_{12}\right)\mathbf{Q}_2, \tag{14}$$

$$\overline{\mathbf{F}}_c = \left(-\Omega^2\mathbf{M}_{11}-i\Omega\mathbf{C}_{11}+\mathbf{K}_{11}\right)\overline{\mathbf{Q}}_1 + \left(-\Omega^2\mathbf{M}_{12}-i\Omega\mathbf{C}_{12}+\mathbf{K}_{12}\right)\overline{\mathbf{Q}}_2, \tag{15}$$

Furthermore, the contact force is expressed as:

$$\begin{aligned}\mathbf{f}_c &= f_n\begin{bmatrix}-\cos(\Omega t+\phi)\\ -\sin(\Omega t+\phi)\end{bmatrix} + f_t\begin{bmatrix}\sin(\Omega t+\phi)\\ -\cos(\Omega t+\phi)\end{bmatrix}\\ &= \frac{1}{2}\begin{bmatrix}-f_n-if_t\\ -f_t+if_n\end{bmatrix}e^{i\phi}e^{i\Omega t} + \frac{1}{2}\begin{bmatrix}f_n+if_t\\ -f_t-if_n\end{bmatrix}e^{-i\phi}e^{-i\Omega t}.\end{aligned} \tag{16}$$

Finally, the normal force and the tangential force can be extracted as:

$$\begin{bmatrix}f_n\\ f_t\end{bmatrix} = -2\mathrm{Re}\left(\mathbf{F}_c e^{-i\phi}\right). \tag{17}$$

If the sliding contact conditions, $f_t/f_n = \mu$ and $f_n > 0$, are satisfied, the motion with forward synchronous rubbing is possible. As the

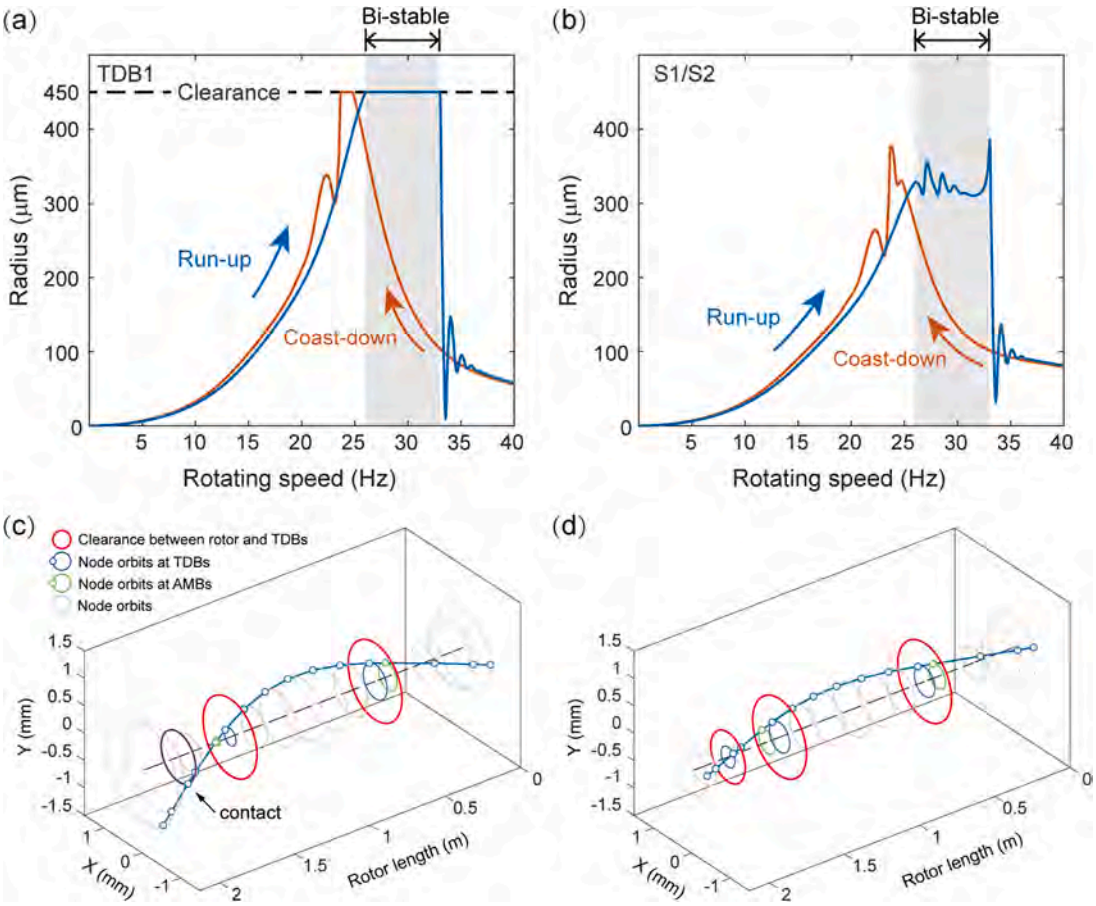

Fig. 9. Simulation results: (a) and (b) radial motion radii of the rotor at TDB1 and S1/S2 plane with gradual increase and decrease of the rotating frequency; (c) and (d) steady-state response of the rotor at 30 Hz during run-up and coast-down, respectively.

phase angle ϕ is undetermined, we need to vary it from 0 to 2π to check if it has a value satisfying the sliding contact conditions.

Fig. 8 shows the calculation results of contact forces from Eq. (17) with the assumption that the node at TDB1 is in contact. At a rotating frequency of 28 Hz, the curve of force ratio f_t/f_n has two points of intersection with $\mu = 0.15$, and the normal force corresponding to $\phi = 0.992$ and $\phi = 2.575$ are positive (81 N and 251.9 N, respectively); hence, a stable rubbing response is possible. At a rotating frequency of 35 Hz, the force ratio f_t/f_n is always less than 0.15 in the range $[0, 2\pi]$; hence, a stable rubbing response is not possible. This agrees with the experimental results shown in Fig. 4.

3.3. Dynamic simulation

This section demonstrates the effectiveness of the established numerical model. First, the acceleration and deceleration processes of the AMB/rotor system (with unbalance mass) were carried out. The rotational frequency was increased from 0 to 40 Hz and then reduced at a similar rate. The radial motion radii of the nodes at TDB1 and S1/S2 plane are shown in Fig. 9(a) and (b). Comparing with the results in Fig. 3, the measured rotor motion radius can be described qualitatively by the numerical model. The rotor responses of the numerical model and experiment facility were consistent with each other, both for the acceleration and deceleration processes. The whirling radius error in the non-contact state is due to the slight bending of the rotor of the test facility. The contact and non-contact regions are obvious. There is a bi-stable region corresponding to Fig. 3 between 26 Hz and 33 Hz. For example, the steady-state response of the rotor after accelerating to 30 Hz is presented in Fig. 9(c) and the node at TDB1 is in persistent contact. While the node at TDB1 is in a non-contact state when the rotor reaches 30 Hz by decelerating. The steady-state non-contact response is shown in Fig. 9(d).

To verify the model further, motions of the rotor when subjected to a shock force at a constant rotational frequency were simulated. Fig. 10(a) and (b) show the simulation of rotor trajectories at S1/S2 plane associated with TDB1 with a rotating frequency of 28 Hz (in the bi-stable zone) in fixed and synchronously rotating reference frames, respectively. In the synchronously rotating reference frame (u, v), a synchronous circular motion will be presented as a point instead of a full orbit. Therefore, the synchronously rotating reference frame (u, v) can present rotor trajectories and phases more clearly. In Fig. 10(a), the rotor experienced transient rebounds that

shiraz.barg@gmail.com

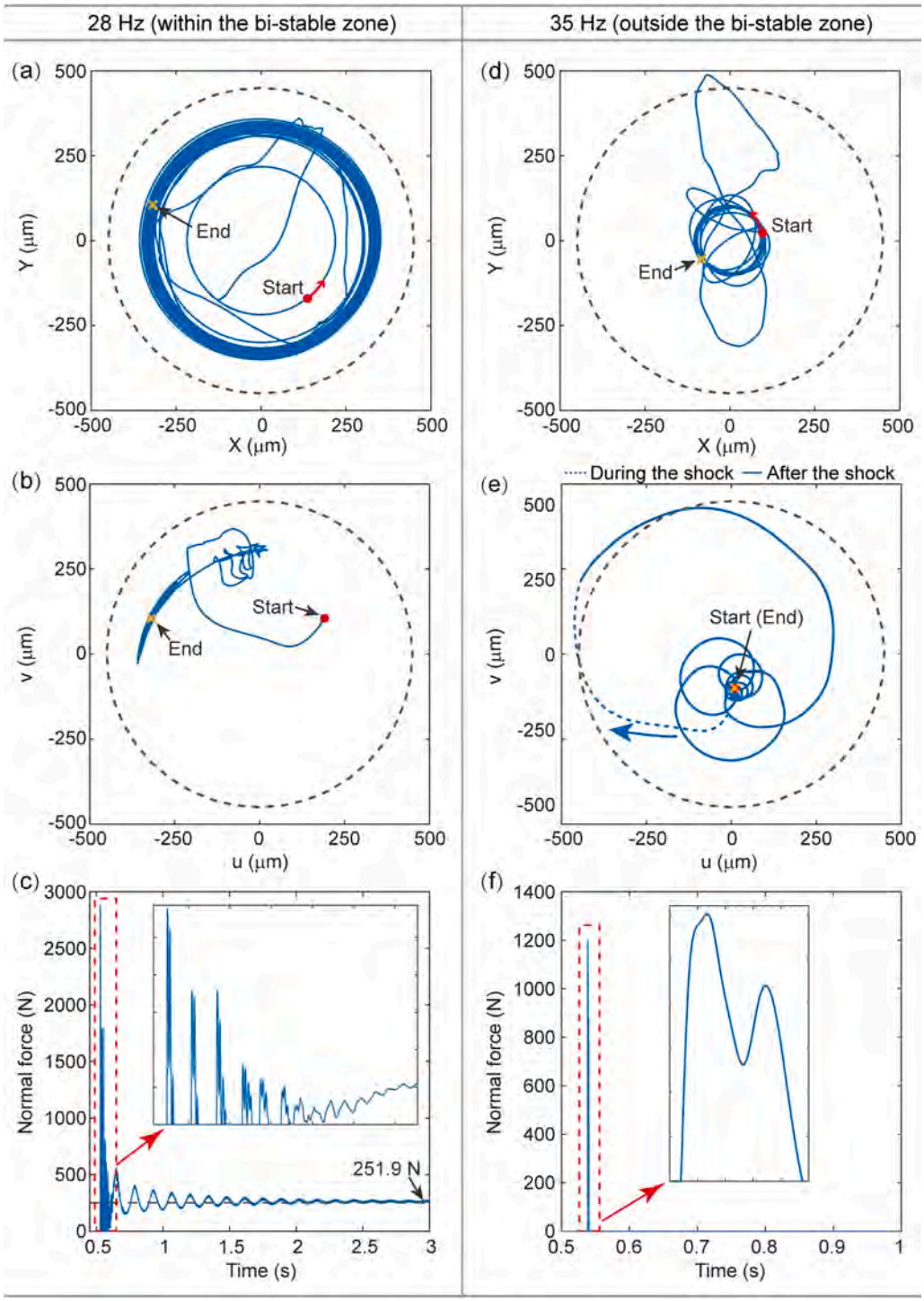

Fig. 10. Simulation of shock responses at S1/S2 plane associated with TDB1 with initial rotational frequencies of 28 Hz and 35 Hz: (a) and (d) rotor trajectories in a fixed reference frame (x, y); (b) and (e) rotor trajectories in a synchronously rotating reference frame (u, v); (c) and (f) normal contact force.

developed into a full forward rub involving persistent contact. In Fig. 10(b), the shock load leads the rotor orbit from the red point to the yellow cross. The persistent synchronous forward whirl is verified as a periodic motion mode in the synchronously rotating reference frame (u, v). Fig. 10(d) and (e) show the simulation of rotor trajectories at TDB1 with a rotating frequency of 35 Hz in fixed and synchronously rotating reference frames, respectively. In Fig. 10(d), the rotor experienced transient rebounds then resumed a non-

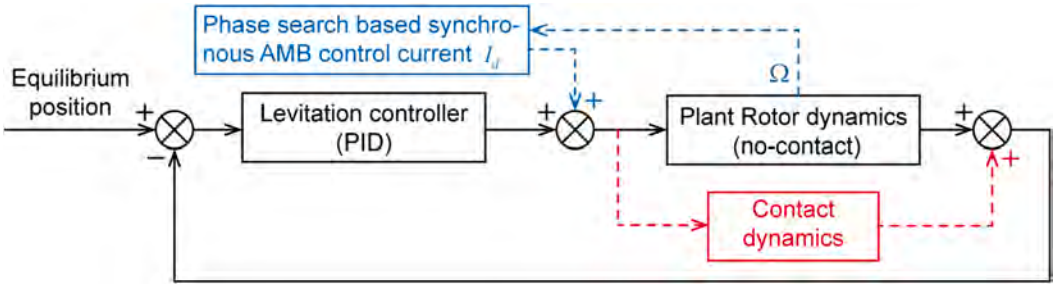

Fig. 11. Open-loop phase search based synchronous compensation (PSSC) control diagram.

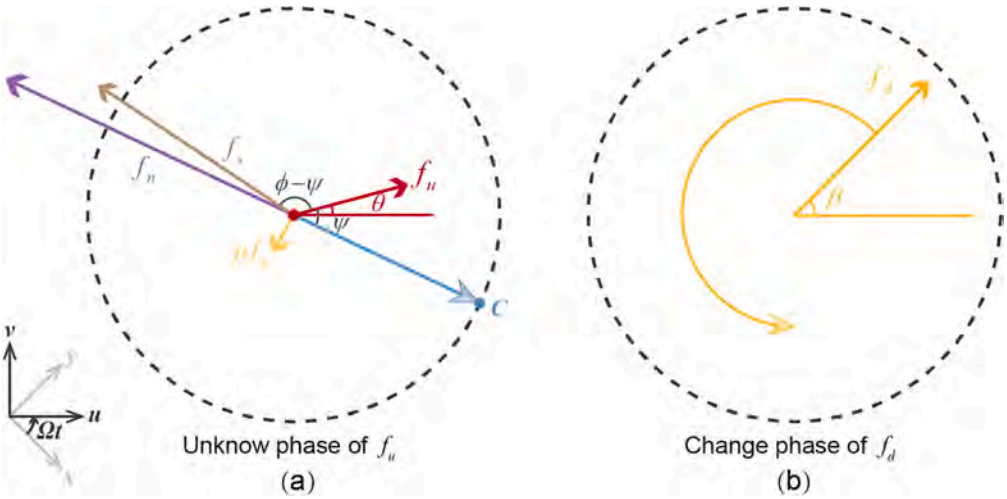

Fig. 12. Problem and strategy of open-loop synchronous control: (a) unknown information about unbalance force f_u; (b) assistant synchronous AMB force vector f_d.

contact whirling motion. In Fig. 10(e), the shock load led the rotor orbit from the red point to the contact status and finally back to the yellow cross. Compared with the results in Fig. 4(a) and (c), this numerical validation provides confidence considering the prediction of the nonlinear dynamic behaviour of the maglev rotor involving a shock contact. In addition, Fig. 10(c) and (f) present corresponding normal contact forces of the rotor. The steady normal contact force of rotor with a rotating frequency of 28 Hz in persistent contact condition fluctuates slightly around 251.9 N, which is in consistent with the result of analytical solution (see Fig. 8). The rotor with a rotating frequency of 35 Hz only experienced a finite time of contact force. Hence, the established numerical model can be used to study impact-rub dynamics and the ensuing re-levitation control algorithm.

4. Re-levitation control

4.1. PSSC control

The desirable course of action to restore a rotor from steady persistent contact is through application of automatic re-levitation control by AMBs (if still functional). Through the above study, the key to re-levitation control is destabilising the force equilibrium in Fig. 1(b).

A simple idea is to use an extra synchronous compensation AMB force f_d that is generated with an open-loop controller (as shown as blue part in Fig. 11)) to destabilise the force equilibrium. The proposed control system (as shown in Fig. 11) consists of two parts. One is levitation control without considering contact between the rotor and TDBs. In a practical industrial application, a PID controller is generally used to achieve this goal. Also, the plant rotor dynamics refer to the dynamic model of the AMB-flexible rotor facility without considering contact. Here, the contact dynamics (the red part in Fig. 11) refer to the interaction dynamics between the rotor and the TDB under contact. The other is the compensation control (blue part in Fig. 11) for destabilizing persistent contact. In this open-loop synchronous control, determining the amplitude and phase of the force f_d is key for the control algorithm. While the analysis of force equilibrium uses the unbalance force vector as the benchmark, prior knowledge for the amplitude f_u and initial phase angle θ (see Fig. 12(a)) of unbalance force may not be available in practical industrial applications. Therefore, the relative phase angle between f_d and the benchmark f_u is hard to obtain, although the initial phase angle β of f_d (in Fig. 12(b)) can be determined by the moment when

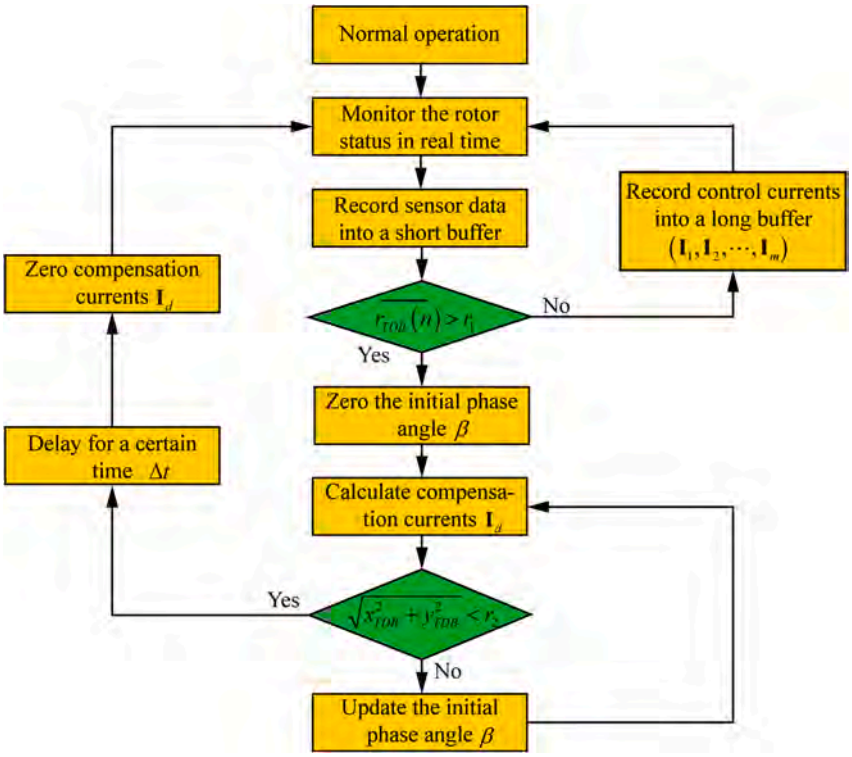

Fig. 13. Control flow chart of PSSC.

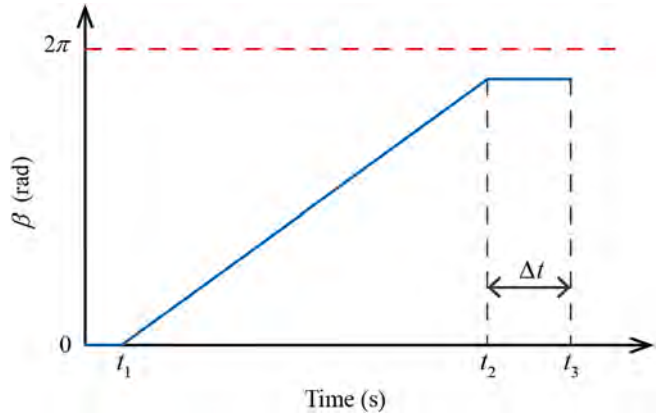

Fig. 14. Update method of phase angle β.

the re-levitation control is applied.

To solve this problem, a phase search based synchronous compensation (PSSC) control is proposed. The control flow chart is presented in Fig. 13.

1. Initially, the rotor status is monitored in real-time, and displacement sensor data at the TDB are recorded into a short buffer at a certain sampling rate.
2. The motion radius $r_{TDB}(n) = \sqrt{x_{TDB}^2(n) + y_{TDB}^2(n)}$ is calculated from the short buffer, and the mean value $\bar{r}_{TDB}(n)$ is compared to r_1. Due to the influence of misalignment, r_1 is generally slightly less than the radial clearance between the rotor and the TDB. If $\bar{r}_{TDB}(n) < r_1$, this means contact does not occur. The control current signals at each pair of coils are recorded into a long buffer as $(\mathbf{I}_1, \mathbf{I}_2, \cdots, \mathbf{I}_m)$ to obtain the control currents in normal operation. Conversely, if $\bar{r}_{TDB}(n) > r_1$, a synchronous compensation current is applied, which is calculated as follows:

shiraz.barg@gmail.com

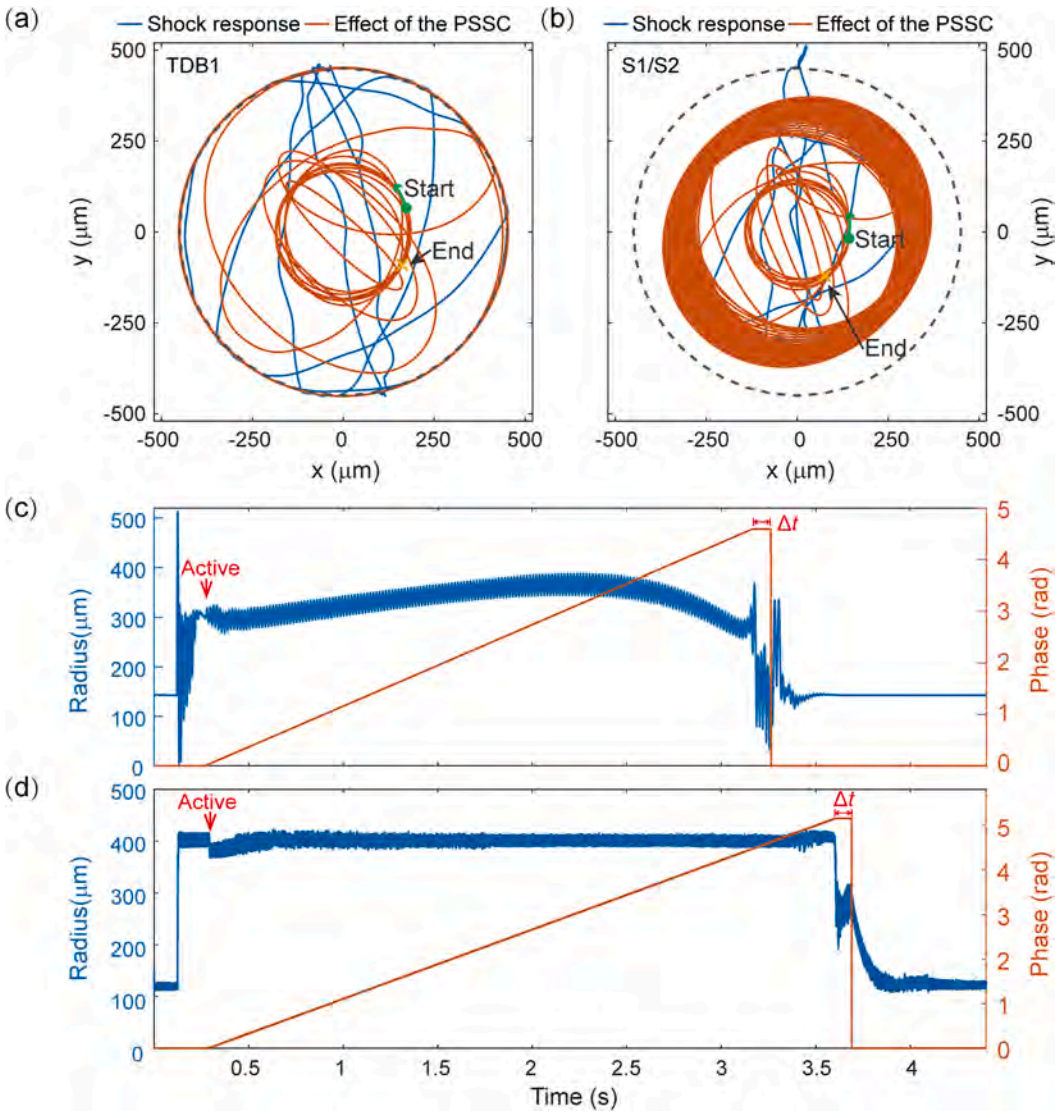

Fig. 15. Simulation and experimental results of the PSSC control: (a) and (b) rotor trajectories at TDB1 and S1/S2 plane in a fixed reference frame (x,y), (c) simulation result and (d) experimental result of rotor motion radii at S1/S2 plane and TDB1.

$$\mathbf{I}_d = \mathbf{I}_m e^{i(\Omega t+\beta)} \tag{18}$$

3. Then, the motion radius of the rotor at TDB is calculated and compared with r_2, which needs to be less than the minimum pulsating motion radius of the rotor in persistent contact status. Generally, r_2 can be set as a middle value between r_1 and the whirling radius in non-contact status. If $\sqrt{x_{TDB}^2+y_{TDB}^2} < r_2$, the synchronous compensation current $\mathbf{I}_d$ will act for a while (Δt) and then return to zero. Otherwise, β updates with a ramp-like change over time, as shown in Fig. 14.

Fig. 15(a) and (b), respectively, show the simulation results of rotor trajectories at TDB1 and S1/S2 plane in a fixed reference frame (x,y), when PSSC control is applied for shock contact. Here, r_1 was set to 290 μm and r_2 to 250 μm. n was set to 1500 as the sampling rate is 10 kHz. The blue line represents the dynamic behaviour of the shock contact process before the action of PSSC control, while the red line represents the dynamic behaviour after the action of PSSC control. Rotor trajectories indicates that the PSSC control restores the rotor orbit from the persistent contact to the non-contact whirl. The corresponding rotor motion radius at S1/S2 plane is drawn in Fig. 15(c). And phase angle β of the synchronous AMB force in this process is also plotted. The rotational frequency was 30 Hz, and the rotor started persistent forward rubbing after experiencing a shock load. After approximately 0.15 s, the PSSC control was activated. However, contact continued, meaning the stability of force equilibrium was not destroyed successfully. Hence, the direction of the

shiraz.barg@gmail.com

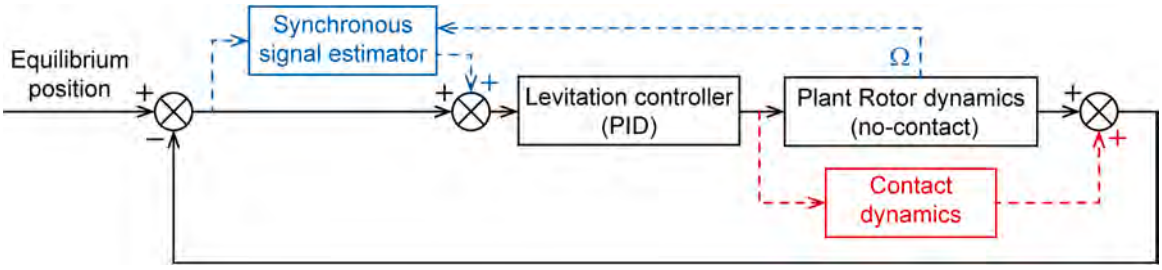

Fig. 16. Synchronous motion compensation (SMC) control diagram.

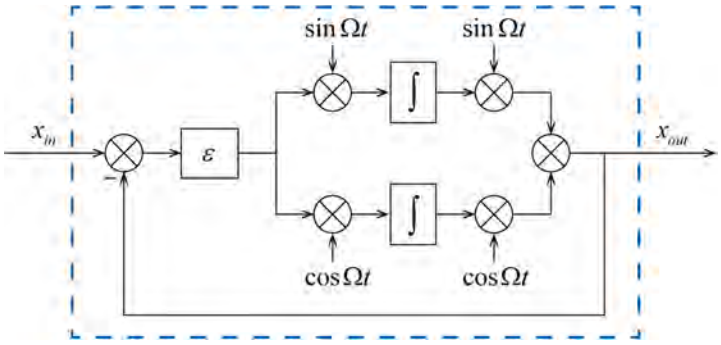

Fig. 17. Synchronous signal estimator.

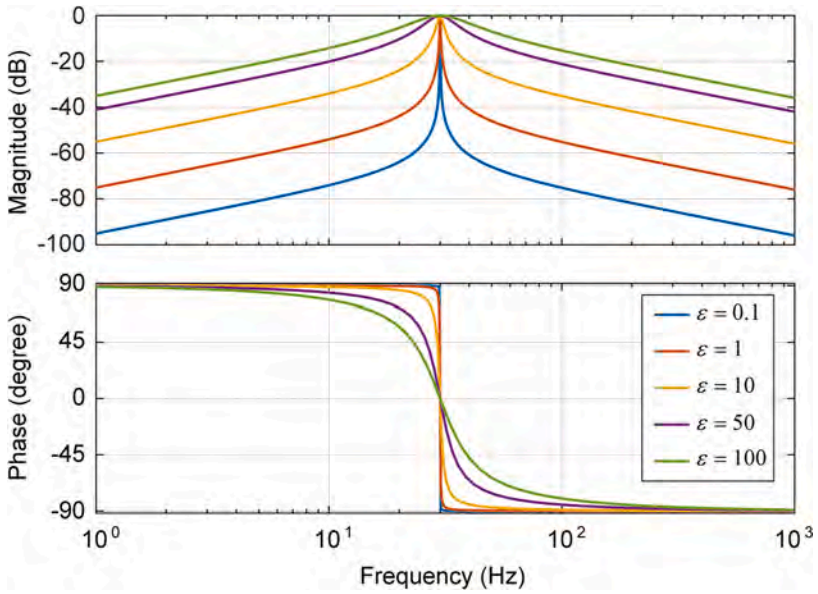

Fig. 18. Magnitude-frequency and phase-frequency diagrams of the synchronous signal estimator with different ε.

synchronous compensation AMB force f_d started to change by searching the phase angle β in a ramp-like way. The radius of rotor motion reduced to below r_2 when β reached 4.59 rad (263°). The synchronous compensation current $\mathbf{I}_d$ acted with this phase angle for 0.1 s and then returned to zero. The rotor recovered under the action of the synchronous compensation current with an appropriate phase.

The experimental results are shown in the Fig. 15(d). Due to measurement noise, the motion radius is the result of the low-pass filtering. Further, the rotor trajectory at TDB1 is not drawn here. There was a slight change on the motion radius of the rotor when the PSSC controller was activated. However, the rotor did not restore immediately. When β reached 5.25 rad (301°) the rotor successfully recovered to non-contact status. The experimental results are basically consistent with the simulation results, verifying the

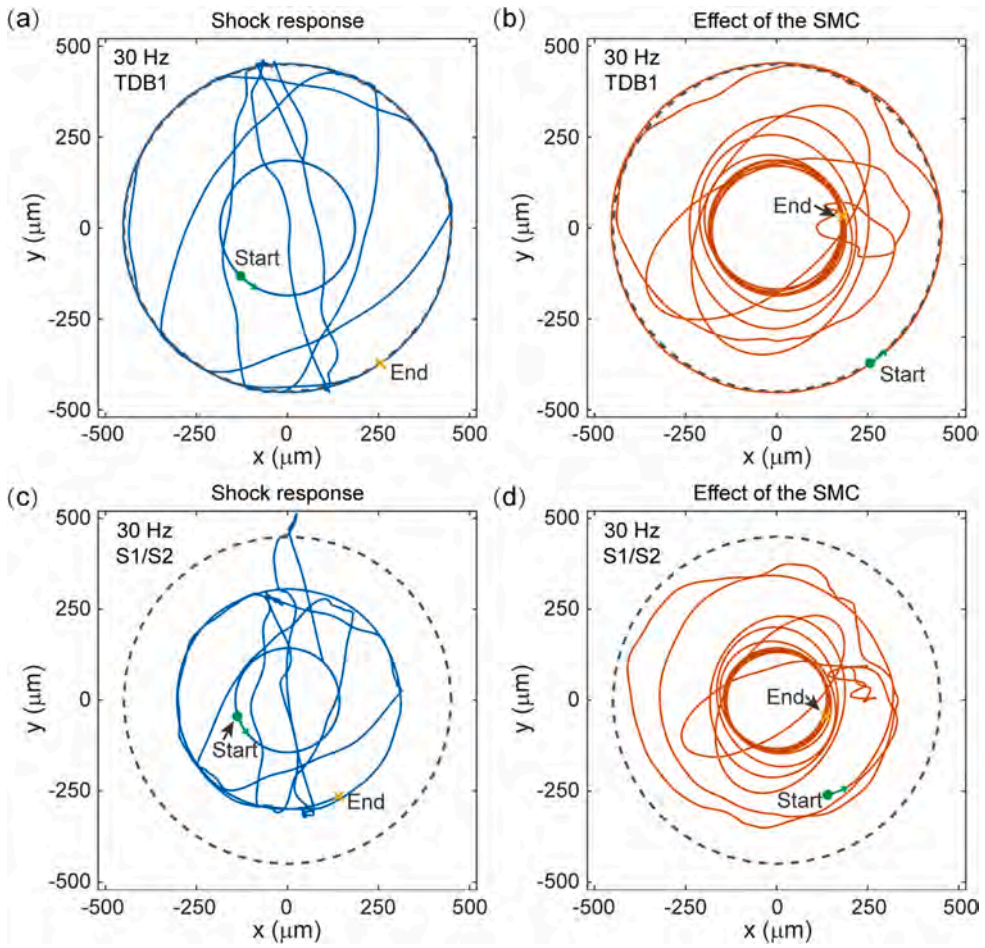

Fig. 19. Rotor trajectories of shock responses and SMC control: (a) and (b) trajectories at TDB1, (c) and (d) trajectories at S1/S2 plane.

effectiveness of the control method. However, the disadvantage is that it may take a certain time to restore the rotor, and the compensation force with an incorrect phase may increase the wear between the rotor and the TDB. To avoid possible prolonged contact, a synchronous signal estimation based synchronous motion compensation (SMC) control was designed in the following section.

4.2. SMC control

Since the feedback signal reflects the phase change caused by the contact, reinforcing synchronous motion feedback signals in the control loop can suppress the synchronous force, which may be another feasible re-levitation control method. Hence, a synchronous signal estimation based SMC control was designed and applied to restore the rotor. The control diagram is shown in Fig. 16.

In the SMC control, a synchronous signal estimator (blue part in Fig. 16) is activated to generate a synchronous motion signal if the contact event (red part in Fig. 16) occurs. The contact detection method is the same as PSSC. The output of the estimator is added to the feedback signal and the current saturation is considered.

The synchronous signal estimator can be a peak filter that is designed based on the Butterworth or other method. However, there is a trade-off between order and calculation speed. Too high order will consume many resources and affect the control bandwidth. In addition, inspired by the research on unbalance vibration suppression [29–31], the block shown in Fig. 17 was applied to realize the estimation of the synchronous signal by limited calculations. The transfer function of the block can be derived as Eq. (19), where Ω is the central frequency and ε determines the filtering depth. The magnitude and phase responses of the synchronous signal estimator with different ε at 30 Hz are shown in Fig. 18. Under the condition that the poles of the control system are all in the right half plane, the block with small ε can generate the center frequency signal with almost no phase lag.

$$H(s) = \frac{\varepsilon s}{s^2 + \varepsilon s + (2\pi\Omega)^2}. \tag{19}$$

To compare the time required for the SMC and the PSSC controls to restore the rotor, the shock contact event and the contact

shiraz.barg@gmail.com

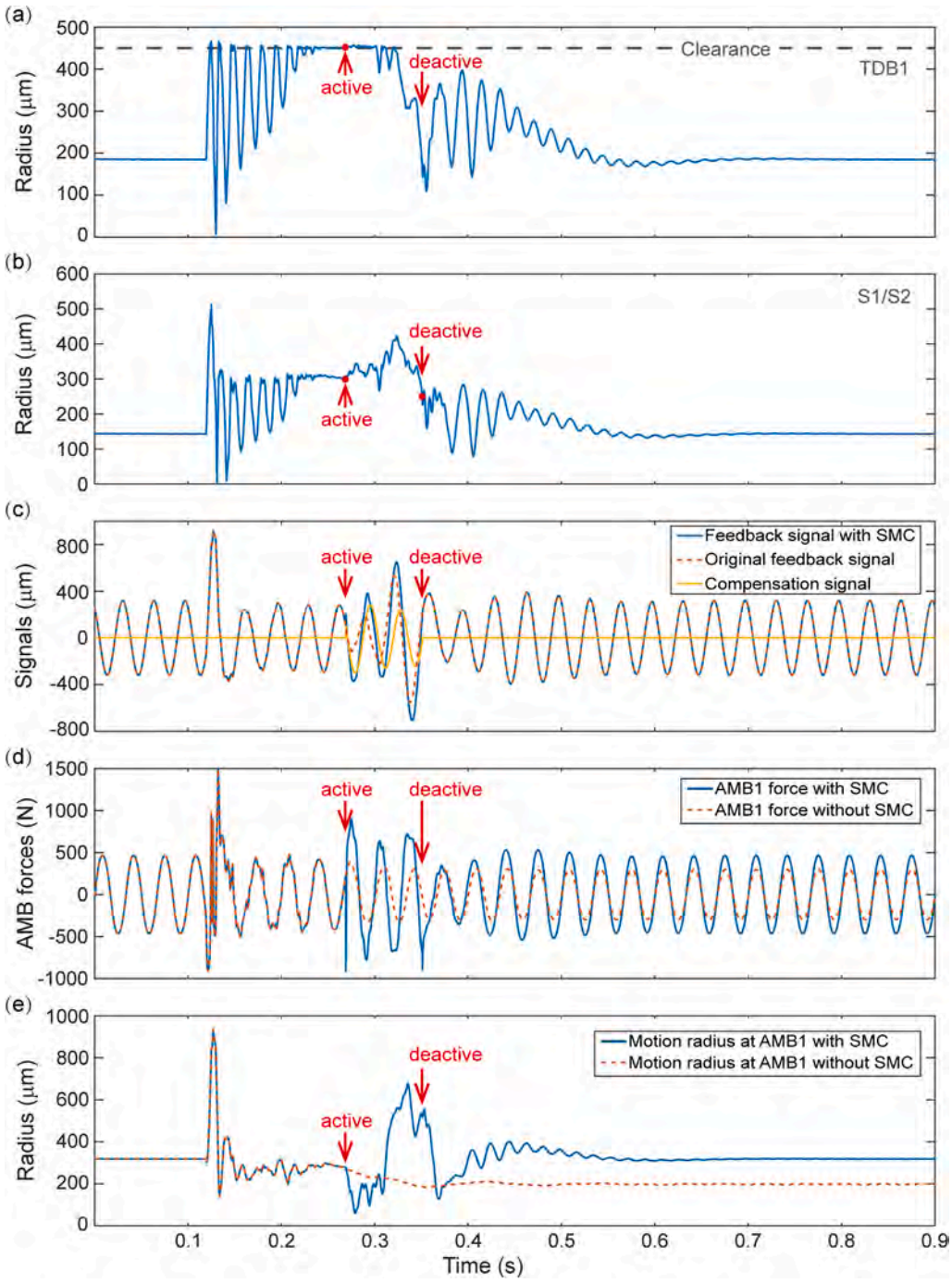

Fig. 20. Simulation results of SMC control. (a) and (b) the motion radii of rotor at TDB1 and S1/S2 plane; (c) feedback signal, original feedback signal, and compensation signal at the *y*-axis of AMB1 with the SMC control; (d) AMB forces of AMB1 in the *y*-axis with/without SMC; (e) the motion radius of rotor at AMB1 with/without SMC.

detection method were the same as the PSSC control and r_1, r_2 were also set as same value. ε was set as 10. Then, the AMB-rotor system with the SMC controller was simulated using the experimental validated numerical model. Like Fig. 15, Fig. 19(a) and (c) show the simulation results of rotor trajectories at TDB1 and S1/S2 plane when shock load was applied. Persistent synchronous forward contact occurred. Fig. 19(b) and (d) show the rotor trajectories at TDB1 and S1/S2 plane when the SMC control was applied for shock contact. The SMC control restored the rotor orbit from the persistent contact to the non-contact whirl. The motion radii of the rotor at TDB1 and S1/S2 plane (as plotted in Fig. 20(a) and (b)) show that the SMC control was activated after approximately 0.15 s of contact. After

Table 1
Comparisons of PSSC and SMC controls.

Items	PSSC control	SMC control
Rotor recovery time	Uncertain, depends on difference between initial and required phases	Out of contact: within 2 whirl cycles
Requirement of calculation speed	Low	Medium or High, may need higher calculation speed of hardware system
Safety	Incorrect phases may further increase the contact force between the TDB and rotor	High

approximately 0.05 s (1.5 whirl cycles), the rotor radius at TDB1 began to drop down, meaning the contact was destabilised successfully. The SMC control ended when the rotor radius at S1/S2 plane dropped below r_2 (250 μm). The rotor recovered to normal operation within 0.5 s after contact, verifying the effectiveness of the SMC control on re-levitation.

To understand the shock contact and re-levitation processes more fully, the feedback signal, original feedback signal, and compensation signal at the *y*-axis of AMB1 for the SMC control are shown in Fig. 20(c). The AMB forces of AMB1 in the *y*-axis with/without SMC are plotted in Fig. 20(d). In Fig. 20(d), it is seen that under PID feedback alone, AMB1 produced a large electromagnetic force, when the shock load was applied. However, it produced a smaller electromagnetic force, when the persistent contact occurred. Although the maximum load of the AMB is large enough to control the rotor, the AMB cannot restore the rotor to be contact-free. The non-collocation between the AMB and the TDB results in a reduction of rotor motion radius at the AMB position in the persistent contact case (as shown as the red dotted line in Fig. 20(e)), which leads to the decrease of the output AMB force under the traditional PID control.

In the SMC re-levitation control, synchronous motion signal compensation of AMB forces can restore the rotor quickly and efficiently. Meanwhile, the small and time-limited compensation force means low energy consumption.

4.3. Comparison

Comparing the PSSC and the SMC controls, they are both open-loop compensation methods that do not affect the original stability of the control system. They both have clear and easy to understand control principles, can be applied online, and can recover the rotor to non-contact status automatically. However, there are some differences between the two methods, as presented in Table 1.

5. Conclusions

The dynamic responses without/with contact behaviour and possible contact faults caused by shock loads in a rotor/AMB/TDB system have been investigated. Bi-stable responses were observed in the run-up and coast-down tests on an AMB-flexible rotor facility. In the bi-stable zone, the experiment demonstrated that the shock load is one of the potential trigger conditions that cause persistent contact and the TDB serious damage. The analytical solution for steady synchronous motions with rubbing was proposed for a general AMB-flexible rotor system with bushing type TDBs and validated by the nonlinear simulations and experiments. A nonlinear dynamic model of the rotor facility was built and validated against the test results. The model successfully reproduced the bi-stable responses and the shock-induced persistent contact phenomenon.

To destabilise persistent contact and restore contact-free levitation, the PSSC control that uses an open-loop synchronous compensation force to destroy the force equilibrium is designed. The phase of the compensation signal increases ramp-like until rotor recovery. The effectiveness of the PSSC control is verified by simulation and experimental results. To avoid possible prolonged contact of the PSSC control, the SMC control, which aims to reinforce synchronous motion feedback signals, is designed and re-levitates the rotor successfully. Finally, detailed similarities and differences between the two control methods are compared. Both control methods can be applied online and recover the rotor automatically without restarting the machine. The PSSC control has a low requirement of calculation speed but incorrect phases may increase the wear of rotor and TDBs. The SMC control has a faster recovery time than the PSSC control but consumes more computing resources.

Future work will focus on the study of the contact dynamics and control of AMB systems with ball bearings as TDBs. New re-levitation control may need to be designed to deal with multi-mode shock responses such as bouncing contact and backward pure rolling.

CRediT authorship contribution statement

Yixin Su: Conceptualization, Methodology, Software, Validation, Investigation, Formal analysis, Data curation, Writing - original draft. **Yongpeng Gu:** Conceptualization, Methodology, Software, Validation, Investigation, Formal analysis, Data curation, Writing - review & editing. **Patrick S. Keogh:** Conceptualization, Methodology, Resources, Writing - review & editing. **Suyuan Yu:** Conceptualization, Resources, Writing - review & editing, Supervision, Funding acquisition. **Gexue Ren:** Conceptualization, Writing - review & editing, Supervision, Project administration.

Declaration of Competing Interest

The authors declare that they have no known competing financial interests or personal relationships that could have appeared to influence the work reported in this paper.

Acknowledgments

This work was supported by the National Key R & D Program of China (Grant No.2018YFB2000100) and the Tsinghua University Initiative Scientific Research Program (Grant No.20193080086). The authors thank Dr. Runan Zhang and Gauthier Fieux from University of Bath for guiding the use of the instrument.

References

[1] R. Siva Srinivas, R. Tiwari, C. Kannababu, Application of active magnetic bearings in flexible rotordynamic systems – a state-of-the-art review, Mech. Syst. Signal Process. 106 (2018) 537–572.
[2] L.A. Hawkins, Shock analysis for a homopolar, permanent magnet bias magnetic bearing system, in: ASME Turbo Expo 1997: Power for Land, Sea and Air, p. V004T14A040.
[3] P.S. Keogh, C. Lusty, N.Y. Bailey, Nonlinear dynamics and control of rotors operating within the clearance gaps of magnetic bearing systems, in: Proceedings of the ASME 2017 International Mechanical Engineering Congress and Exposition, Tampa, Florida, USA, p. V04BT05A012.
[4] P.S. Keogh, M.O.T. Cole, Rotor vibration with auxiliary bearing contact in magnetic bearing systems Part 1 Synchronous dynamics, Proc. Inst. Mech. Eng. Part C 217 (2003) 377–392.
[5] M. Lyu, T. Liu, Z. Wang, S. Yan, X. Jia, Y. Wang, A control method of the rotor re-levitation for different orbit responses during touchdowns in active magnetic bearings, Mech. Syst. Signal Process. 105 (2018) 241–260.
[6] L.A. Hawkins, A. Filatov, S. Imani, D. Prosser, Test results and analytical predictions for rotor drop testing of an active megnetic bearing expander/generator, J. Eng. Gas Turbines Power 129 (2007) 522–529.
[7] O. Halminen, A. Kärkkäinen, J. Sopanen, A. Mikkola, Active magnetic bearing-supported rotor with misaligned cageless backup bearings: a dropdown event simulation model, Mech. Syst. Signal Process. 50 (2015) 692–705.
[8] A. Kärkkäinen, J. Sopanen, A. Mikkola, Dynamic simulation of a flexible rotor during drop on retainer bearings, J. Sound Vib. 306 (2007) 601–617.
[9] P.S. Keogh, M.O.T. Cole, Contact dynamic response with misalignment in a flexible rotor/magnetic bearing system, J. Eng. Gas Turbines Power 128 (2006) 362.
[10] P.S. Keogh, Contact dynamic phenomena in rotating machines: active/ passive considerations, Mech. Syst. Signal Process. 29 (2012) 19–33.
[11] P.S. Keogh, M.O.T. Cole, Dynamic conditions to destabilize persistent Rotor/touchdown bearing contact in AMB systems, Mech. Eng. J. 4 (2017) 1–11.
[12] M. Schlotter, P.S. Keogh, Synchronous position recovery control for flexible rotors in contact with auxiliary bearings, J. Vib. Acoust. 129 (2007) 550.
[13] M. Wang, M.O. Cole, P.S. Keogh, New LMI based gain-scheduling control for recovering contact-free operation of a magnetically levitated rotor, Mech. Syst. Signal Process. 96 (2017) 104–124.
[14] M.O.T. Cole, P.S. Keogh, Rotor vibration with auxiliary bearing contact in magnetic bearing systems Part 2: Robust synchronous control for rotor position recovery, Proc. Inst. Mech. Eng. Part C 217 (2003) 393–409.
[15] L. Ginzinger, H. Ulbrich, Control of a rubbing rotor using an active auxiliary bearing, J. Mech. Sci. Technol. 21 (2007) 851–854.
[16] I.S. Cade, M.N. Sahinkaya, C.R. Burrows, P.S. Keogh, An active auxiliary bearing control strategy to reduce the onset of asynchronous periodic contact modes in rotor/magnetic bearing systems, J. Eng. Gas Turbines Power 132 (2010), 052502.
[17] P. Li, N. Sahinkaya, P. Keogh, Active touchdown bearing control for recovery of contact-Free rotor levitation in AMB systems 2014, in: Proceedings of the 14th International Symposium of Magnetic Bearing, Linz, Austria, pp. 1–6.
[18] C. Jarroux, J. Mahfoud, B. Defoy, T. Alban, Stability of rotating machinery supported on active magnetic bearings subjected to base excitation, J. Vib. Acoust. 142 (2020) 1–7.
[19] C. Jarroux, J. Mahfoud, R. Dufour, F. Legrand, B. Defoy, T. Alban, Dynamic behavior of a rotor-AMB system due to strong base motions, in: Proceedings of the 10th International Conference on Rotor Dynamics – IFToMM 2018, Rio, pp. 340–349.
[20] C. Jarroux, Nonlinear transient dynamics of on-board rotors supported by Active Magnetic Bearings (Ph.D. thesis), University of Lyon, Lyon, 2017.
[21] Y. Su, Y. Gu, P.S. Keogh, S. Yu, G. Ren, Nonlinear dynamic simulation and parametric analysis of a rotor-AMB-TDB system experiencing strong base shock excitations, Mech. Mach. Theory 155 (2021), 104071.
[22] L.A. Hawkins, Z. Wang, K. Nambiar, Floating shock platform testing of a magnetic bearing supported chiller compressor – measurements and simulation results, in: Proceedings of ASME Turbo Expo 2018 Turbomachinery Technical Conference and Exposition, Oslo, Norway, pp. 1–10.
[23] S. Yu, G. Yang, L. Shi, Y. Xu, Application and research of the active magnetic bearing in the nuclear power plant of high temperature reactor, in: Proceedings of 10th International Symposium on Magnetic Bearings, Martigny, Switzerland, pp. 1–7.
[24] G. Yang, Z. Shi, N. Mo, L. Zhao, Research on active magnetic bearing applied in Chinese modular high-temperature gas-cooled reactor, Prog. Nucl. Energy 77 (2014) 352–360.
[25] X. Liu, Z. Shi, G. Yang, X. Yan, Theoretical Research about the Dynamics of a rotor with a decreasing length suspended by active magnetic bearings, in: Proceedings of 25th International Conference on Nuclear Engineering, Shanghai, China, p. V002T03A065.
[26] R.K. Khatri, L.A. Hawkins, C. Bazergui, Demonstrated operability and reliability improvements for a prototype high-speed rotary-disc atomizer supported on active magnetic bearings, in: Proceedings of ASME Turbo Expo 2015: Turbine Technical Conference and Exposition, pp. 1–10.
[27] J. Nelson, H.D. McVaugh, The dynamics of rotor- bearing systems using finite elements, ASME J. Eng. Ind. 98 (1976) 593–600.
[28] M. Lalanne, G. Ferraris, Rotordynamics prediction in engineering, vol. 2, Wiley, 1998.
[29] R. Herzog, P. Bühler, C. Gähler, R. Larsonneur, Unbalance compensation using generalized notch filters in the multivariable feedback of magnetic bearings, IEEE Trans. Control Syst. Technol. 4 (1996) 580–586.
[30] Q. Chen, G. Liu, B. Han, Suppression of imbalance vibration in AMB-rotor systems using adaptive frequency estimator, IEEE Trans. Industr. Electron. 62 (2015) 7696–7705.
[31] Q. Chen, G. Liu, B. Han, Unbalance vibration suppression for AMBs system using adaptive notch filter, Mech. Syst. Signal Process. 93 (2017) 136–150.